Long-term observations of black carbon and carbon monoxide in the Poker Flat Research Range, central Alaska, with a focus on forest wildfire emissions

Takeshi Kinase[1], Fumikazu Taketani[1,2], Masayuki Takigawa[1], Chunmao Zhu[2], Yongwon Kim[3], Petr Mordovskoi[1], and Yugo Kanaya[1,2]

[1]Institute of Arctic Climate and Environment Research, Japan Agency for Marine-Earth Science and Technology (JAMSTEC), Yokohama 2360001, Japan
[2]Earth Surface System Research Center, Research Institute for Global Change, Japan Agency for Marine-Earth Science and Technology (JAMSTEC), Yokohama 2360001, Japan
[3]International Arctic Research Center, University of Alaska Fairbanks (UAF), Fairbanks 757340, U.S.A.

Correspondence to: Takeshi Kinase (tkinase@jamstec.go.jp)

Abstract

Forest wildfires in interior Alaska represent an important black carbon (BC) source for the Arctic and sub-Arctic. However, BC observations in interior Alaska have not been sufficient to constrain the range of existing emissions. Here, we show our observations of BC mass concentrations and carbon monoxide (CO) mixing ratios in the Poker Flat Research Range (65.12° N, 147.43° W), located in central Alaska, since April 2016. The medians of the hourly BC mass concentration and CO mixing ratio throughout the observation period were 13 ng m^{-3} and 124.7 ppb, respectively. Significant peaks in the BC mass concentration and CO mixing ratio were observed at the same time, indicating influences from common sources. These BC peaks coincided with peaks at other comparative sites in Alaska, indicating large BC emissions in interior Alaska. Source estimation by FLEXPART-WRF confirmed a contribution of forest wildfires in Alaska when high BC mass concentrations were observed. For these cases, we found a positive correlation ($r = 0.44$) between the observed BC/ΔCO ratio and fire radiative power (FRP) observed in Alaska and Canada. This finding indicates that the BC and CO emission ratio is controlled by the intensity and time progress of forest wildfires and suggests the BC emission factor or/and inventory could be potentially improved by FRP. We recommend that FRP be integrated into future bottom-up emission inventories to achieve a better understanding of the dynamics of pollutants from frequently occurred forest wildfires under the rapidly changing climate in the Arctic.

1 Introduction

Climate change in the Arctic region has been strongly accelerated compared to the global average (Box et al., 2019; Bonfils et al., 2020). The near-surface air temperature increased between 1.8 and 3.1 °C in the period between 1971 and 2017 (Box et al., 2019). This rapid temperature increase in the Arctic region caused significant decreases in the extent of sea ice (Aizawa et al., 2021), resulting in the acceleration of Arctic warming (Cohen et al., 2014; Thackeray and Hall, 2019). Even if net CO_2 emission is controlled to zero until the end of the 21st century (SSP1-2.6 scenario), modelling studies predicted a more than 3.5 °C temperature increase (Cai et al., 2021; Xie et al., 2022). However, there are still some difficulties associated with climate predictions based on global climate models because of the widespread use of different model hindcasts and forecasts (Overland et al., 2014). Specifically, it is known that the Arctic amplification process causes a significant acceleration in Arctic warming, but the process is highly complicated and is not sufficiently understood; this includes processes involved in aerosol concentration changes and the deposition of black carbon (BC) on snow and ice surfaces (Cohen et al., 2014). Thus, more research is required to understand Arctic climatic processes.

BC aerosols, which are formed by various incomplete combustion processes, such as fossil fuel and biomass burning (Bond et al., 2013), strongly contribute to warming by absorbing solar radiation (Bond et al., 2013; IPCC, 2021). In addition, BC deposited on snow and ice surfaces decreases surface albedo and contributes to snow melting and warming (Aoki et al., 2011; Bond et al., 2013; Oshima et al., 2020; IPCC, 2021). BC can be transported over long distances (estimated lifetimes are 3–6 days globally (Wang et al., 2014; Lund et al., 2018)) and affect the climate and environment of remote regions, such as the Arctic (Wang et al., 2011; Matsui et al., 2022). However, large discrepancies among model estimations for BC climate effects on the Arctic remain (Gliß et al., 2021) because of a lack of observation data (IPCC, 2021) to constrain the models in terms of dependence on emission inventories (Pan et al., 2020; Matsui et al., 2022) and/or removal rates (Ikeda et al., 2017; Lund et al., 2018). For long-range transport from Asia to the Arctic, constraints on the major BC emissions from East Asia (Choi et al., 2020; Kanaya et al., 2020), ship-based observations for BC transport to the Arctic (Taketani et al., 2016, 2022), evaluation of the multimodel bias using these datasets (Whaley et al., 2022) and an improved understanding of transport mechanisms and source attributions (Ikeda et al., 2017; Zhu et al., 2020) have been achieved. However, more observational constraints are required for the characterization of BC emissions from boreal forest wildfires (Pan et al., 2020; AMAP, 2021).

Forest wildfires in the northern American region, especially those that occur in Alaska every summer (Picotte et al., 2020), are one of the important BC emission sources in the Arctic and subarctic troposphere, and they result in depositional fluxes on snow and ice over the Arctic and surrounding regions (Xu et al., 2017; AMAP, 2021; Williamson and Menounos, 2021; Matsui et al., 2022). The occurrences of these forest wildfires in interior Alaska have increased since the 1980s (Sierra-Hernández et al., 2022), and this increasing trend is predicted to continue (Hu et al., 2015; Box et al., 2019; AMAP, 2021); the emission of aerosols, including BC from forest wildfires, is projected to severely affect the environment (Halofsky et al., 2020) and climate (Schmale et al., 2021) in the future.

61 BC mass concentrations have long been observed in the atmosphere and snow at Utqiagvik (Barrow) (Eck et al., 2009; Garrett

62 et al., 2011; Mori et al., 2020), which is a high Arctic coastal tundra site. Campaign studies on atmospheric BC mass

63 concentrations were also conducted in interior Alaska using aircrafts (Kondo et al., 2011b; Bian et al., 2013; Creamean et al.,

64 2018). These campaign observations have provided an in-depth understanding of aerosol parameters related to wildfires.

65 However, separate long-term observations of BC mass concentrations are required to characterize annual trends and seasonality.

66 Fewer studies have reported atmospheric BC mass concentrations in interior and coastal Alaska (Polissar et al., 1996, 1998;

67 Eck et al., 2009; Mouteva et al., 2015) and the high Arctic coastal site (Alert, Canada) (Garrett et al., 2011). To understand the

68 long-term variations in BC mass concentration and their impacts on the climate and environment, more BC observation data

69 from interior Alaska are needed (AMAP, 2011). In this study, we aimed to investigate detailed variations in BC mass

70 concentration and its sources, with a focus on forest wildfires in interior Alaska, based on our monitoring of BC and CO at the

71 Poker Flat Research Range (PFRR), which is a University of Alaska Fairbanks (UAF) observational site in interior Alaska.

72

2 Method

2.1 Observation site

75 We conducted BC and CO monitoring at the PFRR (65.12° N, 147.43° W, 500 m a.s.l.) starting in April 2016. The PFRR is

76 located in the centre of interior Alaska (Figure 1), approximately 35 km northeast of Fairbanks. The PFRR is surrounded by a

77 predominant evergreen needled-leaved (black spruce; *Picea mariana*) forest with shrubland and herbaceous vegetation

78 (Buchhorn et al., 2020). In this study, BC and CO monitoring results were analysed between April 2016 and December 2020.

79
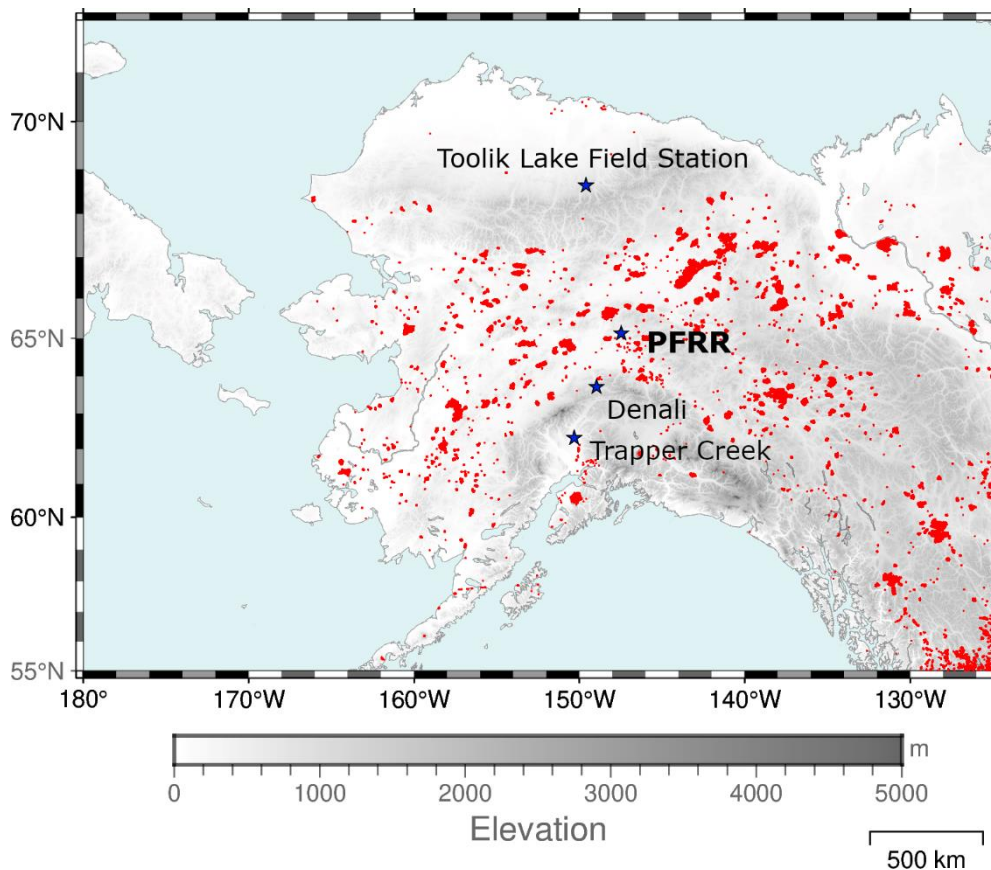
80

81 Figure 1. A map that shows the location of the PFRR and other sites compared in section 3.2 (Trapper Creek, Denali, and

82 Toolik Lake Field Station). All hot spots (larger than 0.3 (MW) in fire radiative power (FRP)) observed in the USA and Canada

83 by the Visible Infrared Imaging Radiometer Suite (VIIRS) between 2016 and 2020 are shown in red colour.

84

85 **2.2 Measurements**

86 BC was measured by a Continuous Soot Monitoring System (BCM3130, Kanomax, Japan) with a flow rate of 0.78 L min^{-1} at

87 standard temperature and pressure (STP; 273 K and 1013 hPa). Sample air was introduced using an approximately 10 m

88 conductive silicone tube (1/2" i.d.) from a height of 5.5 m above the ground. To minimize interferences from scattering particles,

89 coarse mode particles (approximately >1.0 μm), such as mineral dust, were removed by a PM1.0 cyclone (URG-2000-30ED,

90 URG, USA) operated with a small flow regulation pump (~4.5 L min^{-1} at STP). In addition, to remove nonrefractory particles,

91 such as sulfate and organics, the sample air was heated to approximately 300 °C using a heated inlet before it was introduced

92 into the instrument. More details of the instrument are described elsewhere (Miyazaki et al., 2008; Kondo et al., 2009, 2011a).

93 One-minute observation data were averaged to hourly data as the primary data. The limit of detection value (LOD) for hourly

94 BC mass concentration was estimated to be 2 ng m^{-3}, which is the sum of average hourly data and 3-σ values using 18 hours

95 of particle-free air measurements.

96 The CO mixing ratio was measured by an infrared absorption photometer (48iTLE, Thermo Fisher Scientific, USA) with a

97 flow rate of 0.5 L min^{-1}. Sample air was introduced using an approximately 10 m PFA tube from a height of 5.5 m above the

98 ground. Internal zero measurements were carried out for 20 minutes every hour, and the CO mixing ratio was estimated from

99 the difference in absorption between the sample and the zero measurements. Span gas (0.99 ppm CO/N$_2$, Taiyo-Nissan, Tokyo,

100 Japan) calibration was performed in April 2016. We calculated ΔCO as the enhancement in CO from background levels (14

101 days moving 5-percentile values of observation results). Cases with hourly ΔCO larger than 3-σ (13.9 ppb in median, 1-σ was

102 derived from zero mode measurements before and after the hourly ambient air observations) were only used for analysis.

103

104 **2.3 Model calculation**

105 The FLEXPART (FLEXible PARTicle dispersion model)-WRF (Weather Research & Forecast) model was used in backward

106 mode to characterize the source areas and sectors for the sampled air masses at the PFRR. FLEXPART-WRF version 3.3

107 (Brioude et al., 2013) and WRF version 4.4 (Skamarock et al., 2019) were employed for this study. The FLEXPART-WRF

108 model was driven by mass weighted wind fields and perturbation within the PBL calculated by WRF, which covers the

109 Northern Hemisphere with a 45-km horizontal resolution. The ERA5 global reanalysis (Hersbach et al., 2020) was used as the

110 initial and lateral boundary conditions of WRF, and the meteorological field of WRF was also nudged to ERA5 with e-folding

111 times of 3 hours and 12 hours for wind fields and temperature, respectively. Wet deposition is the major removal process for

112 BC, and the deposition process in FLEXPART version 10 (Grythe et al., 2017) was applied to the FLEXPART-WRF model

113 and was used in this study, with values of 10.0, 1.0, 0.9, and 0.1 employed as the collection efficiencies for wet deposition by

114 rain and snow and the activation efficiencies of cloud condensation nuclei (CCN) and ice nuclei (IN) (C_{rain}, C_{snow}, CCN$_{eff}$, and

115 IN$_{eff}$), respectively. The FLEXPART-WRF calculation was conducted every 6 hours from April 2016 to December 2020. For

116 each simulation, 40000 particles were released at 0.5×0.5 degrees (horizontally) and 200 m AGL (vertically) centred at the

117 PFRR. The particles were tracked for 20 days at 6-hour intervals. The primary output of the FLEXPART-WRF backward

118 calculations was the potential emission sensitivity (PES), which expresses the residence time of particles at a given location

119 and is used to characterize the transport pathways of the sampled air masses. The concentration of BC was estimated by

120 multiplying PES and emissions based on a procedure reported by Sauvage et al. (2017). ECLIPSE (Evaluating the Climate

121 and Air Quality Impacts of Short-Lived Pollutants) version 6b (Klimont et al., 2017) and GFED (Global Fire Emission

122 Database) version 4.1 (Daily) (van der Werf et al., 2014) were used as the anthropogenic and biomass burning emissions,

123 respectively. Note that the Chinese BC emissions from ECLIPSE version 6b with the monthly profile of version 5 are certified

124 with downwind atmospheric BC observations (Kanaya et al., 2020), while other bottom-up inventories might result in a factor

125 of ~2 overestimation. The PES fields were calculated with a horizontal resolution of 0.5 × 0.5 degrees. The contribution of

126 particles within 100 m from the surface was considered for the calculation of PES for anthropogenic emissions. The plume

127 height of the GFAS (Global Fire Assimilation System) (Di Giuseppe et al., 2017) was also used for the estimation of the

128 injection height for biomass burning emissions. The fractional contribution of anthropogenic emissions was considered using

129 eight sectors in the ECLIPSE emission, and the anthropogenic and biomass burning emissions were divided into eight regions.

130 The mean age of BC was also estimated by the mean lag time between release and observed time weighted by the amount of

131 emission at each time period within the 20-day backward calculations.

132

133 2.4 Analysis of the effect of forest wildfire on the BC mass concentration at the PFRR

134 We characterized the observed BC/ΔCO ratios, which are known to be valuable indicators of emission sources and combustion

135 conditions (Kondo et al., 2011b; Pan et al., 2017; Selimovic et al., 2019), in terms of fire radiative power (FRP), which accounts

136 for forest fire intensity. To do this, we compared the BC/ΔCO ratio in high BC mass concentration cases observed in summer

137 and FRP observed by the Visible Infrared Imaging Radiometer Suite (VIIR) on the Suomi NPP satellite. Airmasses were traced

138 for 4 days at the most using the Hybrid Single-Particle Lagrangian Integrated Trajectory model (HYSPLIT; Stein et al., 2015))

139 with GDAS1 meteorological datasets (3 h archived 1° × 1° Global Data Assimilation System) from the National Centers for

140 Environmental Prediction (http://ready.arl.noaa.gov/gdas1.php; accessed on 2 November 2023). The calculation started from

141 500 m AGL at the PFRR site, and fire spots were searched along with the trajectories.

142 The BC/ΔCO ratio is also affected by atmospheric processes (Kanaya et al., 2016; Choi et al., 2020), as only BC is lost via

143 wet removal processes. To extract observation results that were not affected by wet removal processes, we used accumulated

144 precipitation along the trajectory (APT) as an indicator of wet removal processes. Previous studies showed that the BC/ΔCO

145 ratio can be significantly changed when APT is larger than 1 mm (Choi et al., 2020; Kanaya et al., 2016; Kondo et al., 2011b).

146 Therefore, the duration for the accumulation of fire spots was shortened when APT reached 1 mm or when the trajectory

147 reached ground level. Rectangles were defined with ±0.5° in the longitudinal direction and ±0.25° in the latitudinal direction

148 centring around hourly air mass positions. Then, the FRP and the number of hot spots were accumulated for individual

149 rectangles over the duration of the trajectories. Finally, the total accumulated FRP (∑FRP) was divided by the detected total

150 spot number to yield an index describing the conditions of fires affecting the observed airmasses. As hot spot datasets, VIIRS

151 375 m (VNP14IMGTML_NRT) archived datasets from the Fire Information for Resource Management System (FIRMS)

152 website (https://earthdata.nasa.gov/firms; accessed on 2 November 2023) were used in this study. The selected confidence

153 levels were 'nominal' or 'high', and the selected type attributed to thermal anomalies was 'presumed vegetation fire'. In

154 addition, we used FRP values greater than 0.3 MW because hot spots smaller than 0.3 MW included outliers (Figure S1). Only

155 hot spots that were observed within the previous 24 hours were considered.

156

3 Results and discussion

3.1 Time series of observed BC and CO concentrations

159 The time series of BC mass concentration and CO mixing ratio are shown in Figure 2, and those of annual median, 10th, and

160 90th percentile values are summarized in Table 1. The hourly median BC mass concentration and 10th and 90th percentile

161 values throughout the observation period were 13, 3, and 56 ng m^{-3}, respectively. No significant increase in annual median BC

162 mass concentration was observed (Table 1). Abrupt peaks (up to 5540 ng m^{-3}) were occasionally observed during summer.

163 This seasonality differed from BC observational reports at Utqiagvik (Barrow), which showed BC mass concentration over

164 the long term using the same instrument (BCM3130) employed in this study (Sinha et al., 2017; Mori et al., 2020). The previous

165 report showed that the BC mass concentration increases in winter and early spring and decreases in summer. These differences

166 are possibly caused by a difference in location. The PFRR is located in interior Alaska, while Barrow is located on the

167 northernmost coast of Alaska, suggesting that large BC emissions occurred around the PFRR.

168 The median, 10th, and 90th percentiles of hourly CO mixing ratios throughout the observation period were 124.7, 99.0, and

169 148.2 ppb, respectively. Similar to BC, significant increases in the annual median CO mixing ratio were not observed, but

170 contrary to the BC mass concentration, the CO mixing ratio showed clear seasonal variation, high in spring (between February

171 and April, 143.5 ppb in the median) and low in summer (July and August, 103.3 ppb in the median) (Figure 2(b)). These

172 observed CO mixing ratios and seasonal variations were consistent with the aircraft observation results (less than 500 m AGL

173 above the PFRR) provided by the NOAA Global Monitoring Laboratory (https://doi.org/10.15138/39HR-9N34; accessed on

174 2 November 2023) (Figure S2) and previous studies that reported the CO mixing ratio at the PFRR (Kasai et al., 2005;

175 Yurganov et al., 1998). In summer, CO peaks coincident with BC mass concentration were found, suggesting a common

176 emission source for both BC and CO.

177

178 Table 1. Annual summary of the observed hourly BC mass concentration and CO mixing ratio at the PFRR.

Year	BC (ng m^{-3})			CO (ppb)		
	Median	10th percentile	90th percentile	Median	10th percentile	90th percentile
2016[a]	11	2	49	109.7	93.1	130.3
2017	15	3	65	128.2	100.5	148.8
2018	14	3	53	118.2	93.3	149.4
2019	15	3	63	128.4	113.1	150.8
2020	13	3	50	131.3	107.5	150.6

179 [a] Observations started on 28 April 2016.

180
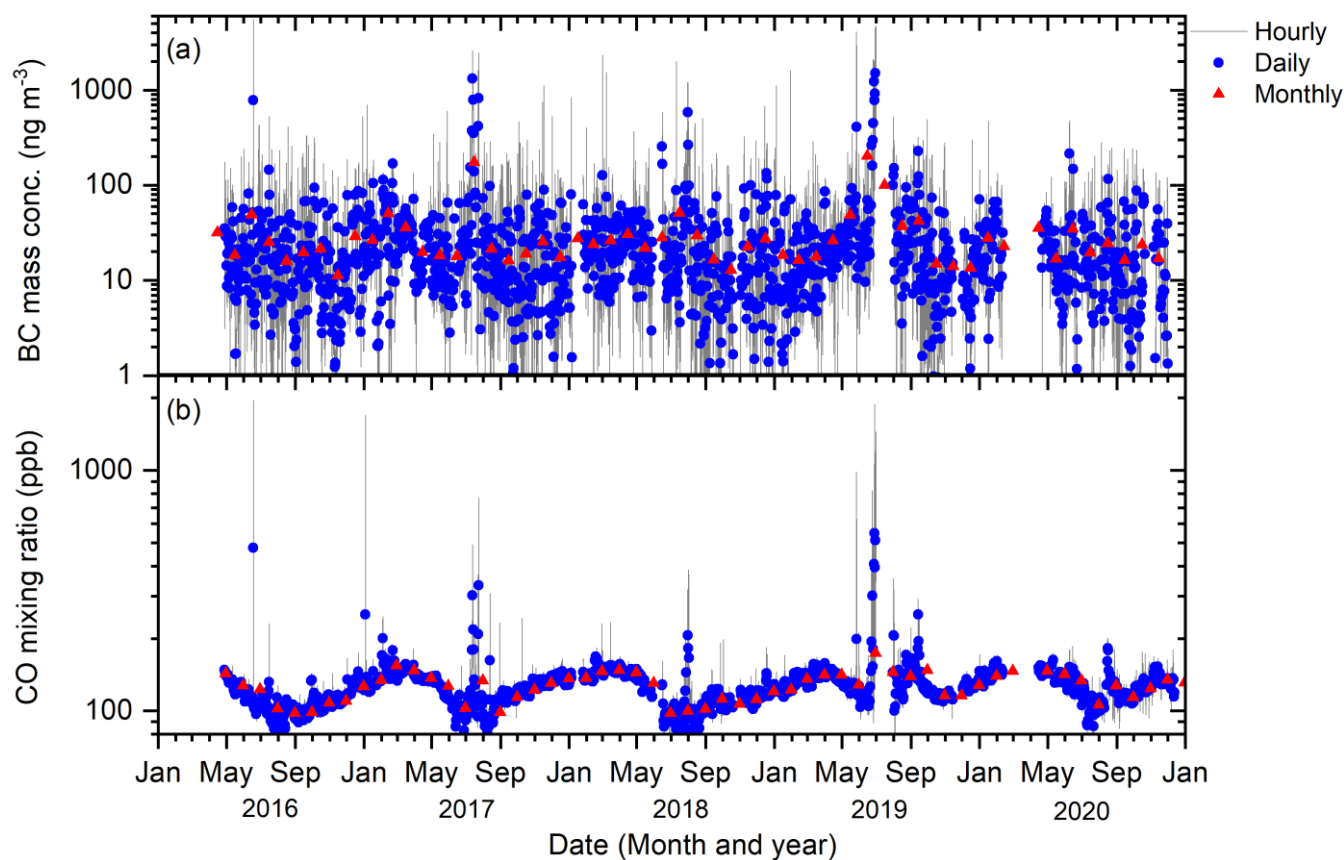
181

182 Figure 2. Time series of (a) BC mass concentration and (b) CO mixing ratio. Grey lines, blue points, and red triangles show

183 hourly, daily, and monthly averages, respectively.

184

3.2 Comparisons with other observation sites

We compared the BC observation results from the PFRR to those from other Alaskan sites (Table 2 and Figure S3), i.e., Trapper Creek (TRCR), Denali (DENA), and Toolik Lake Field Station (TOOL), using datasets for 24-hour filter samples collected every three days. The datasets were from the thermal/optical reflectance method at DENA, TRCR, and TOOL (http://views.cira.colostate.edu/fed/QueryWizard/; accessed on 2 November 2023). A systematic bias might be present in terms of the methods used, but it is most likely within a factor of 2 from the actual conditions based on comparisons with recent data at various sites (Miyazaki et al., 2008; Kondo et al., 2009; Kanaya et al., 2008; Kondo et al., 2011a; Ohata et al., 2021; Sinha et al., 2017). For the BC mass concentration observed at TRCR, DENA, and TOOL, datasets flagged V0 (valid value) were selected.

The BC mass concentration peaks were nearly coincided for the PFRR, DENA, TRCR, and TOOL (Figure S3). The median and maximum daily BC mass concentrations observed at each site are summarized in Table 2. The median BC mass concentrations at DENA, TRCR, and TOOL were larger than those at the PFRR by 6–19 ng m^{-3} (Table 2), but the significance of the difference is unclear considering methodological differences and associated uncertainties (precision). Here, the uncertainties of the thermal/optical reflectance method varied between 12 and 14 ng m^{-3} in median values during the whole observation period. Note that our BC observation, which had a better LOD (2 ng m^{-3}) and higher temporal resolution (1 hour), could provide more reliable data in this low range. On the other hand, the maximum BC mass concentrations were higher at the PFRR within the period with common BC peaks than at TRCR and TOOL but similar at DENA (Table 2). This indicates that significant BC emissions in central Alaska were better captured at the PFRR than at other observation sites. We will discuss source and emission ratio characterization in Sections 3.4 and 3.5 by fully utilizing the superior temporal resolution and accuracy of our observations.

205

Table 2. Summary of site locations and measurement results at PFRR (this study), TRCR, DENA, and TOOL.

Site	Latitude (°N)	Longitude (°W)	Altitude (m a.s.l)	Daily BC mass concentration (ng m^{-3})	
				Median	Maximum
PFRR[a]	65.12	147.43	500	18	920
TRCR	62.32	150.32	155	37	570
DENA	63.73	148.97	658	24	1044
TOOL[b]	68.64	149.61	740	28	643

[a] Data were selected from the same date at PFRR, TRCR, and DENA.

208   [b] Observations started on 13 November 2018.

209

210   **3.3 Comparison of observation and model simulations and possible BC sources**

211   Figure 3(a) shows a time series of 6-hour averages of the observation data and 6-hourly BC mass concentrations estimated by

212   FLEXPART-WRF simulations. FLEXPART-WRF could capture the high BC mass concentration peaks (Figure 3(a)) with a

213   correlation coefficient of 0.7 (Figure S4). The median of the simulated/observed ratio (observation data > LOD in this case)

214   was 1.0 for the whole observation period, indicating good agreement between the model simulation and observations.

215   The source region and source sector contributions derived from the FLEXPART-WRF simulation are shown in Figure 3(b)

216   and (c). Source regions were classified into 8 categories, i.e., Europe, Central Asia, Russia, East Asia, Canada, Alaska, USA

217   (excluding Alaska), and Others (Figure 3(b)). Source sectors were classified into 9 categories, i.e., biomass burning, ship, gas

218   flaring, waste incineration, transport, industry, energy, domestic, and agriculture (Figure 3(c)). The BC source sectors and

219   regions varied significantly according to the season (Figure 3(b) and (c)). In the warm season (between May and September),

220   the possible BC source regions were Russia (3.6–74% in the 10–90 percentile) and Alaska (12–85% in the 10–90 percentile)

221   (Figure 3(b)), and the possible source sector was estimated to be biomass burning (8.1–88% in the 10–90 percentile) (Figure

222   3(c)), especially when BC mass concentration was high, suggesting that BC contributions from biomass burning that occurred

223   in Russia and Alaska are both significant for BC mass concentrations at the PFRR. As snow cover disappears from the ground

224   and the atmospheric conditions become drier, forest wildfires caused by lightning increase in these warm seasons (Reap, 1991;

225   Kaplan and Lau, 2021), resulting in increases in BC emissions from biomass burning (AMAP, 2021). We will focus on these

226   high BC mass concentration cases from Alaska and discuss the relationship between forest wildfire intensity and the BC/ΔCO

227   ratio in the following section.

228   On the other hand, in the cold seasons (between October and April), the domestic (24–48% in the 10–90 percentile) and

229   transport sectors (25–48% in the 10–90 percentile) were estimated to be possible dominant BC source sectors (Figure 3(c)).

230   The dominant source region was Alaska (19–88% in the 10–90 percentile), and occasionally, Russia (0.89–31% in the 10–90

231   percentile) and East Asia (1.2–41% in the 10–90 percentile) were significant (Figure 3(b)).

232
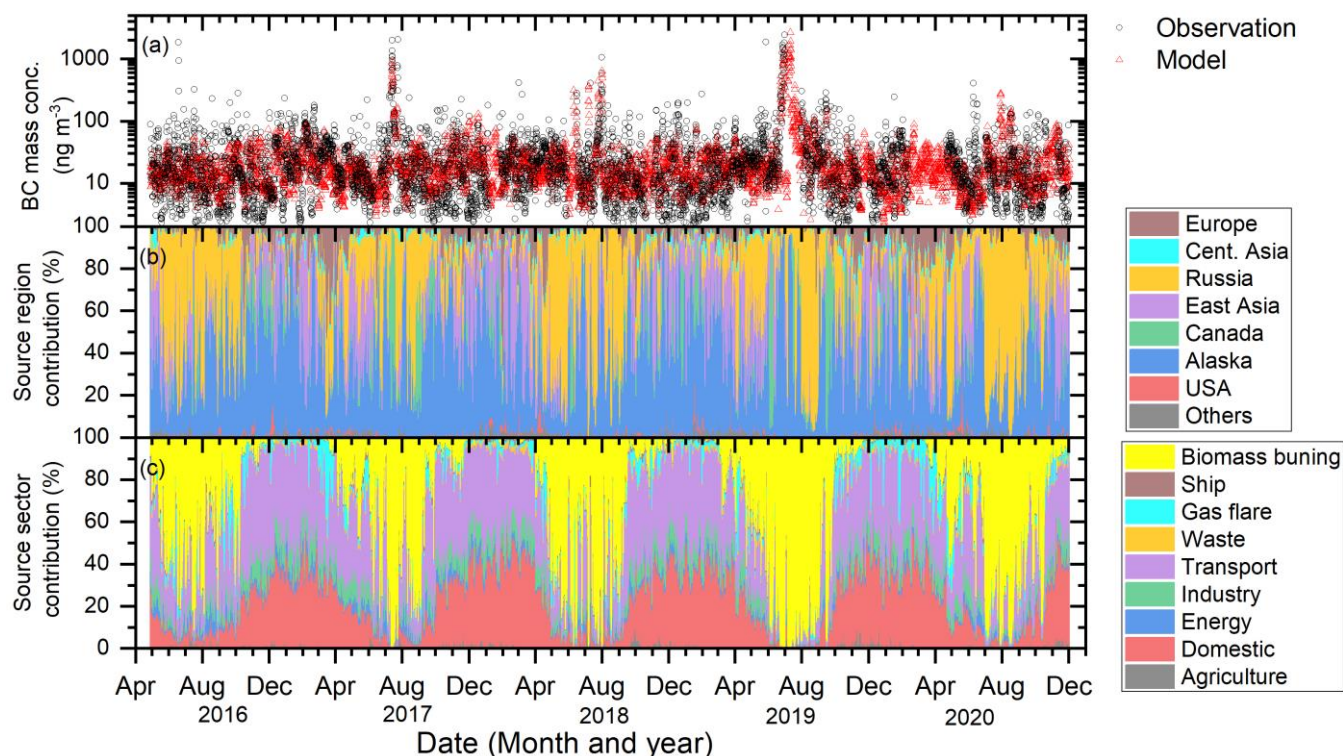
Figure 3. Time series of (a) BC mass concentrations from observations at the PFRR (6-hour average) and FLEXPART-WRF estimates (6 hours). Black circles and red triangles show the observed and simulated BC mass concentrations, respectively. Time series of simulated 6-hourly (b) contributions from BC source regions and (c) contributions from BC source sectors estimated by FLEXPART-WRF simulation. Individual colours show the source regions and sectors.

3.4 Biomass burning contribution for high BC concentration cases

Hereafter, we focus on high BC mass concentration cases at the PFRR (647 hours in total), which were selected with the 98 percentile value (171 ng m^{-3}) as the threshold for the hourly BC mass concentration. The cumulative BC mass concentration observed in these high BC mass concentration cases accounted for 5.7–43% of the annual BC mass concentration, although the duration of these periods was very short (17–187 hours in a year). Most of these high BC concentration cases (approximately 90%) were observed in warm seasons (between June and September) and were related to forest wildfires in Alaska. The median CO mixing ratio for the high BC concentration cases (174.7 ppb) was also significantly higher than that in other periods (124.7 ppb), suggesting that both BC and CO were emitted from forest wildfires (see Section 3.3).

247   The normalized frequency distribution of the BC/ΔCO ratio for the high BC mass concentration cases is shown in Figure 4(a).

248   The median, 10th, and 90th percentile values of the BC/ΔCO ratio during these periods were 4.7, 1.8, and 18 ng m^{-3} ppb^{-1},

249   respectively. These observed BC/ΔCO ratios in the high BC mass concentration cases were in the same range or sometimes

250   higher than those in previous studies that reported the BC/ΔCO ratios from boreal forest wildfire emissions in Canada (Kondo

251   et al., 2011b) and Siberia (Paris et al., 2009; Chi et al., 2013; Vasileva et al., 2017). Increases in biomass burning derived

252   BC/ΔCO ratios with combustion efficiency were suggested from a boreal forest wildfire study (Kondo et al., 2011b) and from

253   laboratory-scale burning experiments of crop residues (Pan et al., 2017); however, in-depth studies examining variabilities in

254   BC/ΔCO ratios based on long-term, near-forest observations have not been conducted. To consider the possibility that

255   combustion conditions (flaming and smouldering) primarily control the BC/ΔCO ratio, we will investigate the relationship

256   between the BC/ΔCO ratio and forest wildfire intensity in the following section.

257   The medians of the contributions of biomass burning and the mean age of BC estimated by the FLEXPART-WRF simulation

258   in these high BC mass concentration cases were higher and shorter (95.5% and 2.6 days) than those in other periods (7.6% and

259   6.9 days) (Figure 4(b) and (c)), indicating a strong contribution of BC from neighbouring forest wildfires. We also calculated

260   the 6-hourly mass-weighted biomass burning contributions from individual source regions (5 categories based on Figure 3(c),

261   Canada and USA are categorized as North America and East Asia, Central Asia, and Europe are included in Others) to the BC

262   mass concentrations at the PFRR (Figure 5). As a result, we found that large peaks, such as those observed between June and

263   August in 2017, 2018, and 2019, coincided well with the peaks of BC contributions from forest wildfires in Alaska. These

264   results confirmed that the observed high BC mass concentration cases were primarily affected by local forest wildfires in

265   Alaska. These peaks were widely observed in Alaska (Section 3.2) and imply a large impact of local forest wildfires on BC

266   mass concentration in this region. However, when these high BC mass concentration cases were selected, the median of the

267   simulated/observed ratio was 0.30, indicating underestimation in the model simulation (possibly due to insufficient spatial

268   resolution for neighbouring forest wildfires and difficulties in representing the vertical profiles of BC emissions) or/and in

269   emission inventories in the high BC mass concentration cases. Several studies have indicated that differences in different

270   inventories cause large uncertainties in model estimates of BC emissions, atmospheric concentrations, and radiative impacts,

271   especially in boreal North America (Carter et al., 2020; Pan et al., 2020). The impact of different inventories on model estimates

272   will be discussed in the future.

273
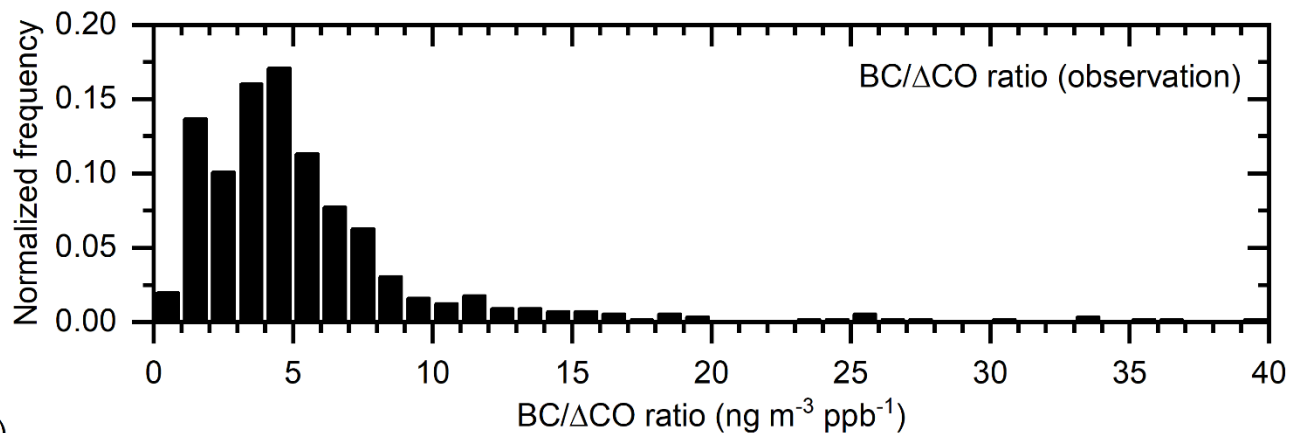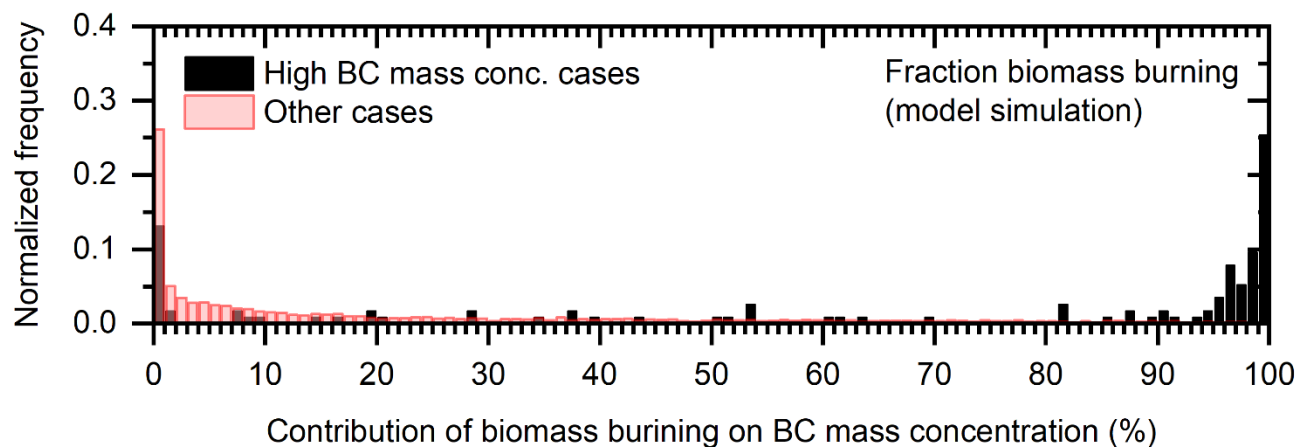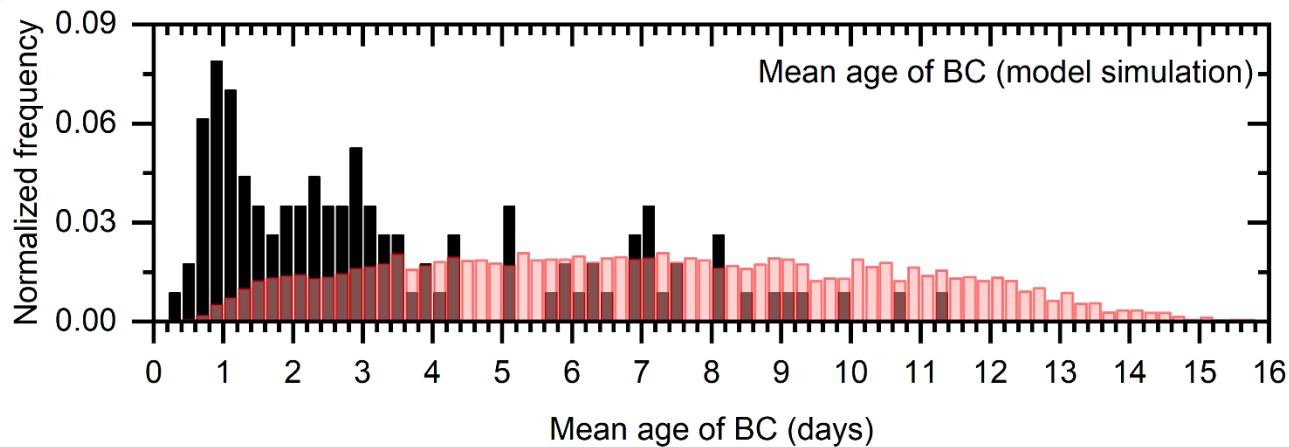
Figure 4. (a) A histogram of the observed BC/ΔCO ratio at the PFRR in high BC mass concentration cases. Histograms of the (b) contributions of biomass burning and (c) mean age of BC simulated with the FLEXPART-WRF model in high BC concentration cases and other cases. Black and red bars used in (b) and (c) indicate high BC concentration cases and other cases, respectively. Hourly results are shown for the observed BC/ΔCO ratio (a), and 6-hourly results are shown for the FLEXPART-WRF simulation ((b) and (c)).
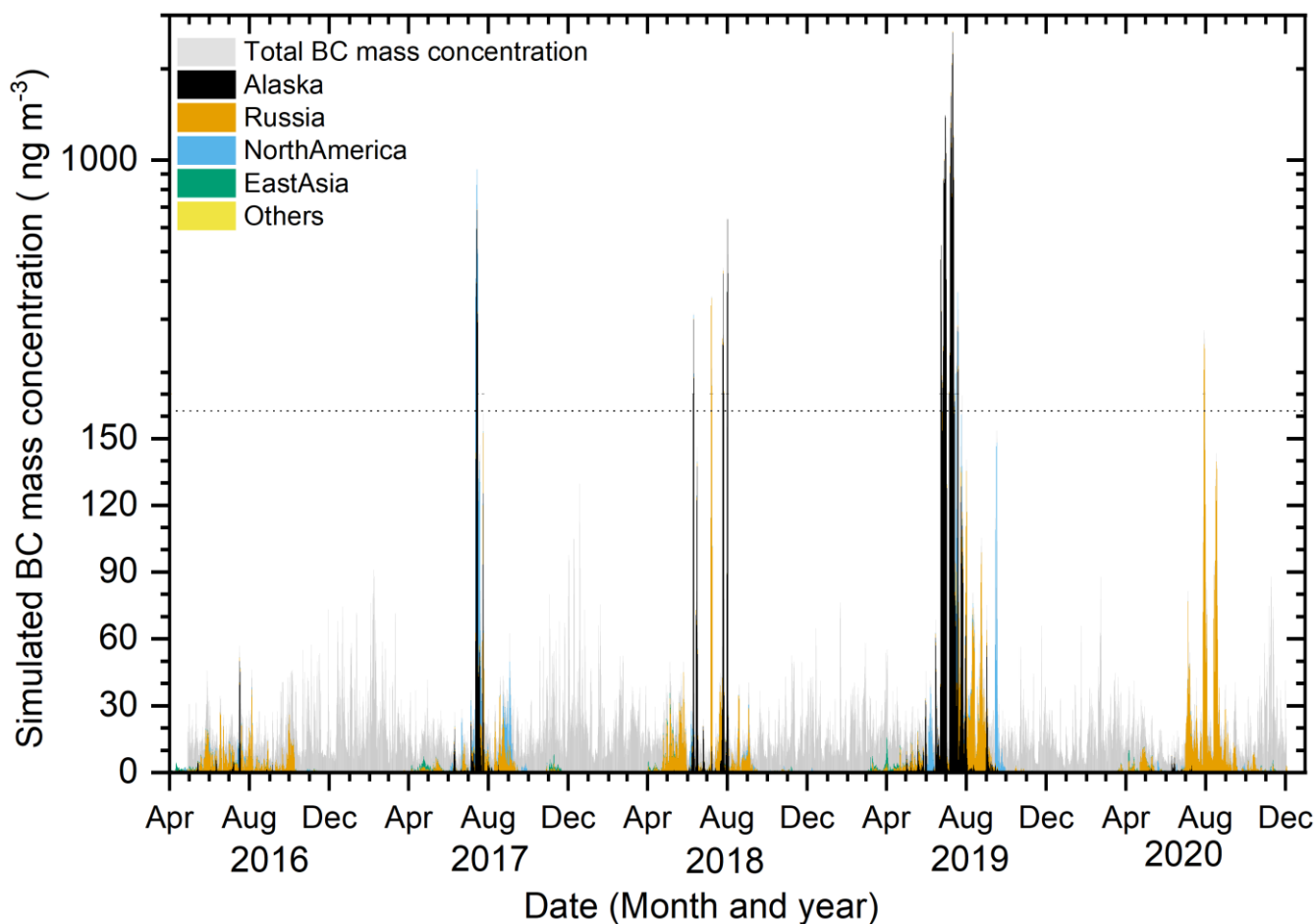
Figure 5. A stacked graph of the 6-hourly mass-weighted biomass burning contributions for BC mass concentration at the PFRR estimated with FLEXPART-WRF simulations. Grey bars indicate the total BC mass concentration for all sources, and the colours show the individual source regions.

3.5 Relationship between the BC/ΔCO ratio and FRP

In the previous section, we showed that most high BC mass concentration cases were related to forest wildfires in Alaska. We selected 406 hourly cases between June and September from the data selected in Section 3.4 as high BC cases from forest wildfires and chose 184 cases of hourly BC observations results from forest wildfires detected in Alaska and western Canada by back trajectory analysis. Note that we also confirmed that no back trajectories could suggest forest wildfires in other seasons. We found a positive correlation ($r = 0.44$, p < 0.0001, n = 184, Figure 6) between the BC/ΔCO ratio and ∑FRP/point values, and its slope and intercept with standard errors were 0.11 (±0.02) and 2.5 (±0.22), respectively (Figure 6). This positive correlation between the BC/ΔCO ratio and ∑FRP/point values, represented for the first time to our knowledge, is qualitatively consistent with previous studies that showed that high combustion efficiency (larger than 0.9 in modified combustion efficiency value (MCE)) increased BC/ΔCO ratios (Selimovic et al., 2019; Kondo et al., 2011b; Pan et al., 2017), which is related to the fact that the BC production process is mostly related to the flaming process (high MCE), while that of CO is related to the smouldering process (low MCE). Although MCE and FRP are different parameters, both parameters indicate combustion conditions and have a strong correlation (Wiggins et al., 2020). Therefore, for the first time, we report a robust correlation between the BC/ΔCO ratio and FRP as a combustion condition indicator. The wide range of BC/ΔCO ratios reported from boreal forest wildfires, from 1.7–3.4 ng m^{-3} ppb^{-1} (Kondo et al., 2011b) to 6.1–6.3 ng m^{-3} ppb^{-1} (Vasileva et al., 2017), could be better explained when the index introduced here (∑FRP/point) is considered. This clear relationship should be taken into account when constructing future emission inventories from boreal forest wildfires.

A positive correlation was found after optimizing the spatial window size (±0.5° in the longitudinal direction and ±0.25° in the latitudinal direction), in which hot spots were taken into account for each hour along the trajectory (from -96 to 0 hours), and the associated time window was used to determine coincident fires that affected the observations (from -24 to 0 hours). The remaining scatter might have arisen from differences in the detection of hot spots in the presence of clouds (Li et al., 2018). To overcome shortcomings in hot spot detection, improvements in the frequency of hot spot scanning should be made, for example, via the use of MODerate Resolution Imaging Spectroradiometer (MODIS) combined with VIIRS observations; it should be noted, however, that there is a significant bias in FRP observations between MODIS and VIIRS, especially for boreal forests (Li et al., 2018). Improvements in the accuracy and consistency of FRP analysis between multiple satellite observations can facilitate a more in-depth understanding of the relationship between FRP and the BC/dCO ratio.

The simulated/observed ratios in high BC mass concentration cases were significantly low (0.30, Section 3.3), contrary to the good agreement observed in overall cases (1.0, Section 3.3). The BC/ΔCO ratios in commonly used emission inventories are 4.4 ng m^{-3} ppb^{-1} for GFED4s (van der Werf et al., 2017) and 4.9 ng m^{-3} ppb^{-1} for Andreae (2019) and are in a range similar to that of our median BC/ΔCO ratio. However, our observed BC/ΔCO ratios in high BC concentration cases for forest wildfires had a broad range between 1.7 and 7.3 ng m^{-3} ppb^{-1} at the 10 and 90 percentiles (median was 4.2 ng m^{-3} ppb^{-1}), respectively, related to the ∑FRP/point values. This indicates that the BC emission factors from biomass burning could vary depending on

318 the FRP. Our findings suggest the potential for improving BC emission inventories and/or emission factors by using FRP. The

319 frequency of boreal forest fires may increase in the future (Box et al., 2019; Hu et al., 2015); as a result, their impact on climate

320 and air quality might become more severe in Alaska and the Arctic (Kim et al., 2005; Schmale et al., 2018; Stohl et al., 2006).

321 Our long-term observations of BC and CO at an hourly temporal resolution in the interior of Alaska provide unique information

322 to test model simulations and emission inventories relevant to the climate and air quality of the Arctic.

323
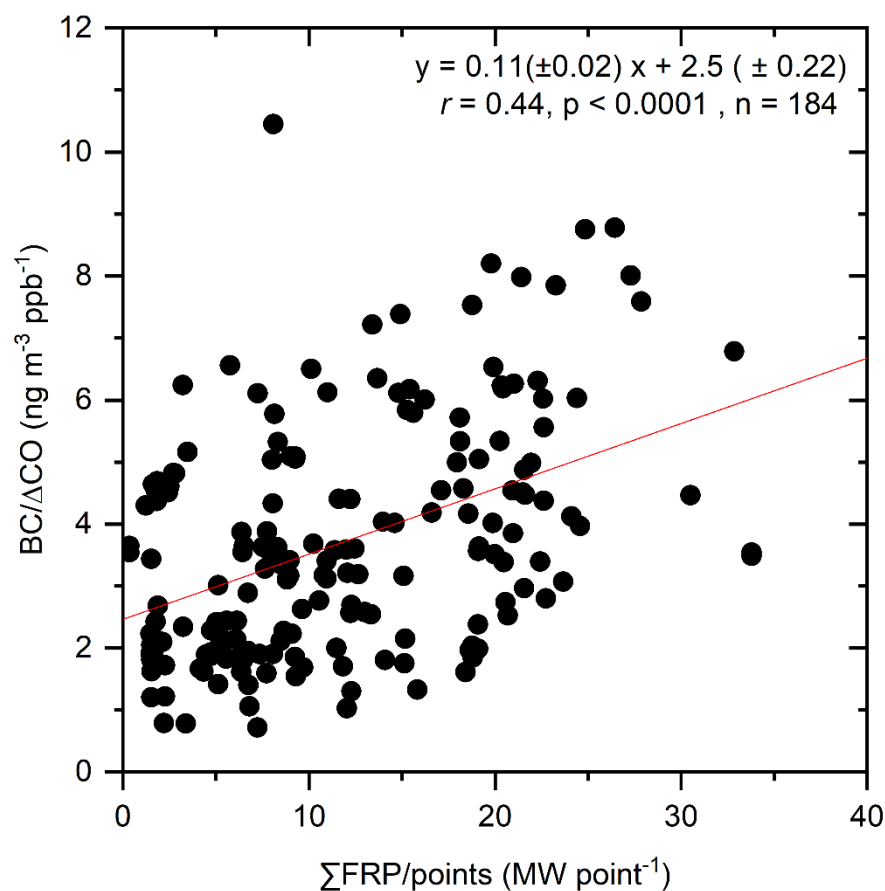
324

325 Figure 6. Correlation between the BC/ΔCO ratio in the high BC mass concentration cases observed at the PFRR and

326 $\sum$FRP/point values. The linear regression curve is shown by a red line.

327

4 Conclusion

We showed key features of the BC and CO concentrations observed at the PFRR in interior Alaska since 2016 in this paper. The annual medians of the BC mass concentration and CO mixing ratio were 11–15 ng m^{-3} and 109.7–131.3 ppb, respectively. Large and short-term increases in BC mass concentrations were sometimes observed between June and September. A clear seasonal variation was observed in the CO mixing ratio, which was high in spring (between February and April, 143.5 ppb in the median) and low in summer (July and August, 103.3 ppb in the median). The CO mixing ratio coincided with the high BC mass concentration peaks, suggesting a strong contribution from forest wildfires to BC and CO concentrations.

The BC mass concentrations observed at other sites in Alaska, i.e., DENA, TRCR, and TOOL, were compared with our results. The annual median BC mass concentrations at the PFRR were lower than those at TRCR, DENA, and TOOL, but coinciding BC mass concentration peaks were found at these observation sites. In these high BC mass concentration cases, BC mass concentrations at the PFRR were larger than those at TRCR and TOOL but similar at DENA, indicating that significant BC emissions from forest wildfires occurred in interior Alaska and affected broad areas in Alaska.

The dominance of forest wildfires in Alaska as a major cause of high BC mass concentration was also supported by the model simulations. We simulated BC mass concentration using the FLEXPART-WRF model and compared the simulations with the observation results. The model simulation could capture observational results (r = 0.70) in which the median simulated/observed ratio was 1.0. The estimated BC source sectors and regions were biomass burning from Russia and Alaska between June and September, while those for other periods were domestic sources and transport and were mainly from Alaska. When we focused on high BC mass concentration cases (greater than 98 percentile values), we found that forest wildfires occurring in Alaska were the dominant source of BC in those cases from the model simulation results. The mean ages of BC and biomass burning contributions in these high BC mass concentration cases estimated by FLEXPART-WRF were 2.6 days and 95.5%, respectively, relatively shorter and higher than those in other cases (6.9 days and 7.6%, respectively). The peaks of the calculated biomass burning contributions from Alaska to BC mass concentrations at the PFRR coincided well with observed and simulated peaks in high BC mass concentration cases, suggesting that the forest wildfires that occurred around the PFRR are significant.

The median observed BC/ΔCO ratio in high BC mass concentration cases related to forest wildfires was 4.2 ng m^{-3} ppb^{-1} and was in the same range as that in previous studies reporting the BC/ΔCO ratio of boreal forest wildfire emissions. Finally, we tracked airmass origin for 4 days using the HYSPLIT model in these cases and investigated the relationship between the observed BC/ΔCO ratio and FRP, which was normalized by the number of hot spots (points) observed by VIIRS. A positive correlation was found between these parameters (r = 0.44), with a slope and intercept of 0.11 (±0.02) and 2.5 (±0.22), respectively. For the first time, the properties of the BC/ΔCO ratio from boreal forest wildfires were systematically characterized in terms of FRP, suggesting the potential to improve emission inventories and/or emission factors by using FRP.

Data availability

The BC and CO observation results at the PFRR site are available from the corresponding author upon request. We used public data for BC observation results at Denali, Trapper Creek, and Toolik Lake Field Station (http://views.cira.colostate.edu/fed/QueryWizard/).

Supplement

The supplement related to this article is available online at https://doi.org/xxxxxxxx.

Author contributions

TK, FT, CZ, YK, and YK conducted and recorded observations for BC and CO at the PFRR site. MT conducted the FLEXPART-WRF model simulations. YK assisted in the fieldwork at the PFRR site. TK, FT, MP, and YK summarized the observation results, and TK wrote the first draft with MT. All authors contributed to the discussion and writing of the manuscript.

Competing interests

At least one of the (co-)authors is a member of the editorial board of Atmospheric Chemistry and Physics.

Acknowledgement

The authors acknowledge technical support from Dr. Takuma Miyakawa, a researcher at JAMSTEC and help with field work from Dr. Hideki Kobayashi, a researcher at JAMSTEC. The authors also thank all the supporting members at JAMSTEC. The authors thank NOAA ARL for providing the HYSPLIT model and GDAS1 meteorological data. We also thank the IMPROVE network. IMPROVE is a collaborative association of state, tribal, and federal agencies and international partners. The US Environmental Protection Agency is the primary funding source, with contracting and research support from the National Park Service. The Air Quality Group at the University of California, Davis, was the central analytical laboratory, and carbon analysis was carried out by the Desert Research Institute. We also thank the anonymous reviewers for their precise and valuable comments that greatly improved the paper.

Financial support

This work was funded by the Arctic Challenge for Sustainability II (ArCS II), Program Grant Number JPMXD1420318865, the Arctic Challenge for Sustainability (ArCS), Program Grant Number JPMXD1300000000, and a National Research Foundation of Korea Grant from the Korean Government (MSIT; the Ministry of Science and ICT, NRF-2021M1A5A1065425) (KOPRI-PN23011).

References

Aizawa, T., Ishii, M., Oshima, N., Yukimoto, S., and Hasumi, H.: Arctic warming and associated sea ice reduction in the early 20th century induced by natural forcings in MRI-ESM2.0 climate simulations and multimodel analyses, Geophys. Res. Lett., 48, https://doi.org/10.1029/2020gl092336, 2021.

AMAP: The Impact of Black Carbon on Arctic Climate, Arctic Monitoring and Assessment Programme (AMAP), 2011.

AMAP: AMAP Assessment 2021:Impacts of Short-lived Climate Forcers on Arctic Climate, Air Quality, and Human Health, Arctic Monitoring and Assessment Programme (AMAP), 2021.

Aoki, T., Kuchiki, K., Niwano, M., Kodama, Y., Hosaka, M., and Tanaka, T.: Physically based snow albedo model for calculating broadband albedos and the solar heating profile in snowpack for general circulation models, J. Geophys. Res., 116, https://doi.org/10.1029/2010jd015507, 2011.

Bian, H., Colarco, P. R., Chin, M., Chen, G., Rodriguez, J. M., Liang, Q., Blake, D., Chu, D. A., Silva, A. da, Darmenov, A. S., and Others: Source attributions of pollution to the Western Arctic during the NASA ARCTAS field campaign, Atmos. Chem. Phys., 13, 4707–4721, 2013.

Bond, T. C., Doherty, S. J., Fahey, D. W., Forster, P. M., Berntsen, T., DeAngelo, B. J., Flanner, M. G., Ghan, S., Kärcher, B., Koch, D., Kinne, S., Kondo, Y., Quinn, P. K., Sarofim, M. C., Schultz, M. G., Schulz, M., Venkataraman, C., Zhang, H., Zhang, S., Bellouin, N., Guttikunda, S. K., Hopke, P. K., Jacobson, M. Z., Kaiser, J. W., Klimont, Z., Lohmann, U., Schwarz, J. P., Shindell, D., Storelvmo, T., Warren, S. G., and Zender, C. S.: Bounding the role of black carbon in the climate system: A scientific assessment, J. Geophys. Res., 118, 5380–5552, https://doi.org/10.1002/jgrd.50171, 2013.

Bonfils, C. J. W., Santer, B. D., Fyfe, J. C., Marvel, K., Phillips, T. J., and Zimmerman, S. R. H.: Human influence on joint changes in temperature, rainfall and continental aridity, Nat. Clim. Chang., 10, 726–731, https://doi.org/10.1038/s41558-020-0821-1, 2020.

Box, J. E., Colgan, W. T., Christensen, T. R., Schmidt, N. M., Lund, M., Parmentier, F.-J. W., Brown, R., Bhatt, U. S., Euskirchen, E. S., Romanovsky, V. E., and Others: Key indicators of Arctic climate change: 1971--2017, Environ. Res. Lett., 14, 045010, 2019.

Brioude, J., Arnold, D., Stohl, A., Cassiani, M., Morton, D., Seibert, P., Angevine, W., Evan, S., Dingwell, A., Fast, J. D., Easter, R. C., Pisso, I., Burkhart, J., and Wotawa, G.: The Lagrangian particle dispersion model FLEXPART-WRF version 3.1, Geosci. Model Dev., 6, 1889–1904, https://doi.org/10.5194/gmd-6-1889-2013, 2013.

420 Buchhorn, M., Smets, B., Bertels, L., De Roo, B., Lesiv, M., Tsendbazar, N.-E., Herold, M., and Fritz, S.: Copernicus Global
421 Land Service: Land Cover 100m: collection 3: epoch 2019: Globe, https://doi.org/10.5281/zenodo.3939050, 2020.

422 Cai, Z., You, Q., Wu, F., Chen, H. W., Chen, D., and Cohen, J.: Arctic Warming Revealed by Multiple CMIP6 Models:
423 Evaluation of Historical Simulations and Quantification of Future Projection Uncertainties, J. Clim., 34, 4871–4892,
424 https://doi.org/10.1175/JCLI-D-20-0791.1, 2021.

425 Carter, T. S., Heald, C. L., Jimenez, J. L., Campuzano-Jost, P., Kondo, Y., Moteki, N., Schwarz, J. P., Wiedinmyer, C.,
426 Darmenov, A. S., da Silva, A. M., and Kaiser, J. W.: How emissions uncertainty influences the distribution and radiative
427 impacts of smoke from fires in North America, Atmos. Chem. Phys., 20, 2073–2097, https://doi.org/10.5194/acp-20-2073-
428 2020, 2020.

429 Chi, X., Winderlich, J., Mayer, J.-C., Panov, A. V., Heimann, M., Birmili, W., Heintzenberg, J., Cheng, Y., and Andreae, M.
430 O.: Long-term measurements of aerosol and carbon monoxide at the ZOTTO tall tower to characterize polluted and pristine
431 air in the Siberian taiga, Atmos. Chem. Phys., 13, 12271–12298, https://doi.org/10.5194/acp-13-12271-2013, 2013.

432 Choi, Y., Kanaya, Y., Takigawa, M., Zhu, C., Park, S.-M., Matsuki, A., Sadanaga, Y., Kim, S.-W., Pan, X., and Pisso, I.:
433 Investigation of the wet removal rate of black carbon in East Asia: Validation of a below-and in-cloud wet removal scheme in
434 FLEXible PARTicle (FLEXPART) model v10. 4, Atmos. Chem. Phys., 20, 13655–13670, 2020.

435 Cohen, J., Screen, J. A., Furtado, J. C., Barlow, M., Whittleston, D., Coumou, D., Francis, J., Dethloff, K., Entekhabi, D.,
436 Overland, J., and Jones, J.: Recent Arctic amplification and extreme mid-latitude weather, Nat. Geosci., 7, 627–637,
437 https://doi.org/10.1038/ngeo2234, 2014.

438 Creamean, Maahn, and Boer: The influence of local oil exploration and regional wildfires on summer 2015 aerosol over the
439 North Slope of Alaska, Atmos. Clim. Sci., 2018.

440 Di Giuseppe, F., Rémy, S., Pappenberger, F., and Wetterhall, F.: Combining fire radiative power observations with the fire
441 weather index improves the estimation of fire emissions, Atmos. Chem. Phys. Disc., https://doi.org/10.5194/acp-2017-790-
442 RC1, 2017.

443 Eck, T. F., Holben, B. N., Reid, J. S., Sinyuk, A., Hyer, E. J., O'Neill, N. T., Shaw, G. E., Vande Castle, J. R., Chapin, F. S.,
444 Dubovik, O., Smirnov, A., Vermote, E., Schafer, J. S., Giles, D., Slutsker, I., Sorokine, M., and Newcomb, W. W.: Optical
445 properties of boreal region biomass burning aerosols in central Alaska and seasonal variation of aerosol optical depth at an
446 Arctic coastal site, J. Geophys. Res., 114, https://doi.org/10.1029/2008jd010870, 2009.

447 Garrett, T. J., Brattström, S., and Sharma, S.: The role of scavenging in the seasonal transport of black carbon and sulfate to
448 the Arctic, Geophys. Res. Lett., https://doi.org/10.1029/2011GL048221, 2011.

449 Gliß, J., Mortier, A., Schulz, M., Andrews, E., Balkanski, Y., Bauer, S. E., Benedictow, A. M. K., Bian, H., Checa-Garcia, R.,
450 Chin, M., and Others: AeroCom phase III multi-model evaluation of the aerosol life cycle and optical properties using ground-
451 and space-based remote sensing as well as surface in situ observations, Atmos. Chem. Phys., 21, 87–128, 2021.

452 Grythe, H., Kristiansen, N. I., Groot Zwaaftink, C. D., Eckhardt, S., Ström, J., Tunved, P., Krejci, R., and Stohl, A.: A new
453 aerosol wet removal scheme for the Lagrangian particle model FLEXPART v10, Geosci. Model Dev., 10, 1447–1466,
454 https://doi.org/10.5194/gmd-10-1447-2017, 2017.

455 Halofsky, J. E., Peterson, D. L., and Harvey, B. J.: Changing wildfire, changing forests: the effects of climate change on fire
456 regimes and vegetation in the Pacific Northwest, USA, Fire Ecology, 16, 4, https://doi.org/10.1186/s42408-019-0062-8, 2020.

Hersbach, H., Bell, B., Berrisford, P., Hirahara, S., Horányi, A., Muñoz-Sabater, J., Nicolas, J., Peubey, C., Radu, R., Schepers, D., Simmons, A., Soci, C., Abdalla, S., Abellan, X., Balsamo, G., Bechtold, P., Biavati, G., Bidlot, J., Bonavita, M., Chiara, G., Dahlgren, P., Dee, D., Diamantakis, M., Dragani, R., Flemming, J., Forbes, R., Fuentes, M., Geer, A., Haimberger, L., Healy, S., Hogan, R. J., Hólm, E., Janisková, M., Keeley, S., Laloyaux, P., Lopez, P., Lupu, C., Radnoti, G., Rosnay, P., Rozum, I., Vamborg, F., Villaume, S., and Jean-Noël Thépaut: The ERA5 global reanalysis, Quart. J. Roy. Meteor. Soc., 146, 1999–2049, https://doi.org/10.1002/qj.3803, 2020.

Hu, F. S., Higuera, P. E., Duffy, P., Chipman, M. L., Rocha, A. V., Young, A. M., Kelly, R., and Dietze, M. C.: Arctic tundra fires: natural variability and responses to climate change, Front. Ecol. Environ., 13, 369–377, https://doi.org/10.1890/150063, 2015.

Ikeda, K., Tanimoto, H., Sugita, T., Akiyoshi, H., Kanaya, Y., Zhu, C., and Taketani, F.: Tagged tracer simulations of black carbon in the Arctic: transport, source contributions, and budget, Atmos. Chem. Phys., 17, 10515–10533, https://doi.org/10.5194/acp-17-10515-2017, 2017.

IPCC: Climate change 2021: the physical science basis, edited by: Masson-Delmotte, V., Zhai, P., Pirani, A., Connors, S. L., Péan, C., Berger, S., Caud, N., Chen, Y., Goldfarb, L., Gomis, M. I., and Others, Cambridge University Press Cambridge, UK, 2021.

Kanaya, Y., Komazaki, Y., Pochanart, P., Liu, Y., Akimoto, H., Gao, J., Wang, T., and Wang, Z.: Mass concentrations of black carbon measured by four instruments in the middle of Central East China in June 2006, Atmos. Chem. Phys., 8, 7637–7649, https://doi.org/10.5194/acp-8-7637-2008, 2008.

Kanaya, Y., Pan, X., Miyakawa, T., Komazaki, Y., Taketani, F., Uno, I., and Kondo, Y.: Long-term observations of black carbon mass concentrations at Fukue Island, western Japan, during 2009--2015: constraining wet removal rates and emission strengths from East Asia, Atmos. Chem. Phys., 16, 10689–10705, 2016.

Kanaya, Y., Yamaji, K., and Miyakawa, T.: Rapid reduction in black carbon emissions from China: evidence from 2009–2019 observations on Fukue Island, Japan, Atmos. Chem. Phys., 2020.

Kaplan, J. O. and Lau, K. H.-K.: The WGLC global gridded lightning climatology and time series, Earth Syst. Sci. Data, 13, 3219–3237, https://doi.org/10.5194/essd-13-3219-2021, 2021.

Kasai, Y. J., Koshiro, T., Endo, M., Jones, N. B., and Murayama, Y.: Ground-based measurement of strato–mesospheric CO by a FTIR spectrometer over Poker Flat, Alaska, Adv. Space Res., 35, 2024–2030, https://doi.org/10.1016/j.asr.2005.04.099, 2005.

Kim, Y., Hatsushika, H., Muskett, R. R., and Yamazaki, K.: Possible effect of boreal wildfire soot on Arctic sea ice and Alaska glaciers, Atmos. Environ., 39, 3513–3520, https://doi.org/10.1016/j.atmosenv.2005.02.050, 2005.

Klimont, Z., Kupiainen, K., Heyes, C., Purohit, P., Cofala, J., Rafaj, P., Borken-Kleefeld, J., and Schöpp, W.: Global anthropogenic emissions of particulate matter including black carbon, Atmos. Chem. Phys., 17, 8681–8723, https://doi.org/10.5194/acp-17-8681-2017, 2017.

Kondo, Y., Sahu, L., Kuwata, M., Miyazaki, Y., Takegawa, N., Moteki, N., Imaru, J., Han, S., Nakayama, T., Oanh, N. T. K., Hu, M., Kim, Y. J., and Kita, K.: Stabilization of the Mass Absorption Cross Section of Black Carbon for Filter-Based Absorption Photometry by the use of a Heated Inlet, Aerosol Sci. Technol., 43, 741–756, https://doi.org/10.1080/02786820902889879, 2009.

Kondo, Y., Sahu, L., Moteki, N., Khan, F., Takegawa, N., Liu, X., Koike, M., and Miyakawa, T.: Consistency and traceability of black carbon measurements made by laser-induced incandescence, thermal-optical transmittance, and filter-based photo-absorption techniques, Aerosol Sci. Technol., 45, 295–312, https://doi.org/10.1080/02786826.2010.533215, 2011a.

Kondo, Y., Matsui, H., Moteki, N., Sahu, L., Takegawa, N., Kajino, M., Zhao, Y., Cubison, M. J., Jimenez, J. L., Vay, S., Diskin, G. S., Anderson, B., Wisthaler, A., Mikoviny, T., Fuelberg, H. E., Blake, D. R., Huey, G., Weinheimer, A. J., Knapp, D. J., and Brune, W. H.: Emissions of black carbon, organic, and inorganic aerosols from biomass burning in North America and Asia in 2008, J. Geophys. Res., 116, https://doi.org/10.1029/2010jd015152, 2011b.

Li, F., Zhang, X., Kondragunta, S., and Csiszar, I.: Comparison of fire radiative power estimates from VIIRS and MODIS observations, J. Geophys. Res., 123, 4545–4563, https://doi.org/10.1029/2017jd027823, 2018.

Lund, M. T., Samset, B. H., Skeie, R. B., Watson-Parris, D., Katich, J. M., Schwarz, J. P., and Weinzierl, B.: Short Black Carbon lifetime inferred from a global set of aircraft observations, npj Climate and Atmospheric Science, 1, 1–8, https://doi.org/10.1038/s41612-018-0040-x, 2018.

Matsui, H., Mori, T., Ohata, S., Moteki, N., Oshima, N., Goto-Azuma, K., Koike, M., and Kondo, Y.: Contrasting source contributions of Arctic black carbon to atmospheric concentrations, deposition flux, and atmospheric and snow radiative effects, Atmos. Chem. Phys., 22, 8989–9009, 2022.

Miyazaki, Y., Kondo, Y., Sahu, L. K., Imaru, J., Fukushima, N., and Kano, M.: Performance of a newly designed continuous soot monitoring system (COSMOS), J. Environ. Monit., 10, 1195–1201, https://doi.org/10.1039/b806957c, 2008.

Mori, T., Kondo, Y., Ohata, S., Zhao, Y., Sinha, P. R., Oshima, N., Matsui, H., Moteki, N., and Koike, M.: Seasonal variation of wet deposition of black carbon in arctic Alaska, J. Geophys. Res., 125, https://doi.org/10.1029/2019jd032240, 2020.

Mouteva, G. O., Czimczik, C. I., Fahrni, S. M., Wiggins, E. B., Rogers, B. M., Veraverbeke, S., Xu, X., Santos, G. M., Henderson, J., Miller, C. E., and Randerson, J. T.: Black carbon aerosol dynamics and isotopic composition in Alaska linked with boreal fire emissions and depth of burn in organic soils, Global Biogeochem. Cycles, 29, 1977–2000, https://doi.org/10.1002/2015gb005247, 2015.

Ohata, S., Mori, T., Kondo, Y., Sharma, S., Hyvärinen, A., Andrews, E., Tunved, P., Asmi, E., Backman, J., Servomaa, H., and Others: Estimates of mass absorption cross sections of black carbon for filter-based absorption photometers in the Arctic, Atmos. Meas. Tech., 14, 6723–6748, 2021.

Oshima, N., Yukimoto, S., Deushi, M., Koshiro, T., Kawai, H., Tanaka, T. Y., and Yoshida, K.: Global and Arctic effective radiative forcing of anthropogenic gases and aerosols in MRI-ESM2.0, Prog. Earth Planet. Sci., 7, 38, https://doi.org/10.1186/s40645-020-00348-w, 2020.

Overland, J. E., Wang, M., Walsh, J. E., and Stroeve, J. C.: Future Arctic climate changes: Adaptation and mitigation time scales, Earths Future, 2, 68–74, https://doi.org/10.1002/2013ef000162, 2014.

Pan, X., Kanaya, Y., Taketani, F., Miyakawa, T., Inomata, S., Komazaki, Y., Tanimoto, H., Wang, Z., Uno, I., and Wang, Z.: Emission characteristics of refractory black carbon aerosols from fresh biomass burning: a perspective from laboratory experiments, Atmos. Chem. Phys., 17, 13001–13016, https://doi.org/10.5194/acp-17-13001-2017, 2017.

Pan, X., Ichoku, C., Chin, M., Bian, H., Darmenov, A., Colarco, P., Ellison, L., Kucsera, T., da Silva, A., Wang, J., Oda, T., and Cui, G.: Six global biomass burning emission datasets: intercomparison and application in one global aerosol model, Atmos. Chem. Phys., 20, 969–994, https://doi.org/10.5194/acp-20-969-2020, 2020.

531 Paris, J.-D., Stohl, A., Nédélec, P., Arshinov, M. Y., Panchenko, M. V., Shmargunov, V. P., Law, K. S., Belan, B. D., and
532 Ciais, P.: Wildfire smoke in the Siberian Arctic in summer: source characterization and plume evolution from airborne
533 measurements, Atmos. Chem. Phys., 9, 9315–9327, https://doi.org/10.5194/acp-9-9315-2009, 2009.

534 Picotte, J. J., Bhattarai, K., Howard, D., Lecker, J., Epting, J., Quayle, B., Benson, N., and Nelson, K.: Changes to the
535 Monitoring Trends in Burn Severity program mapping production procedures and data products, Fire Ecology, 16, 16,
536 https://doi.org/10.1186/s42408-020-00076-y, 2020.

537 Polissar, A. V., Hopke, P. K., Malm, W. C., and Sisler, J. F.: The ratio of aerosol optical absorption coefficients to sulfur
538 concentrations, as an indicator of smoke from forest fires when sampling in polar regions, Atmos. Environ., 30, 1147–1157,
539 https://doi.org/10.1016/1352-2310(95)00334-7, 1996.

540 Polissar, A. V., Hopke, P. K., and Malm, W. C.: Atmospheric aerosol over Alaska: 1. Spatial and seasonal variability, J.
541 Geophys. Res., https://doi.org/10.1029/98JD01365, 1998.

542 Reap, R. M.: Climatological Characteristics and Objective Prediction of Thunderstorms over Alaska, Weather Forecast., 6,
543 309–319, https://doi.org/10.1175/1520-0434(1991)006<0309:CCAOPO>2.0.CO;2, 1991.

544 Sauvage, B., Fontaine, A., Eckhardt, S., Auby, A., Boulanger, D., Petetin, H., Paugam, R., Athier, G., Cousin, J.-M., Darras,
545 S., and Others: Source attribution using FLEXPART and carbon monoxide emission inventories: SOFT-IO version 1.0, Atmos.
546 Chem. Phys., 17, 15271–15292, 2017.

547 Schmale, J., Arnold, S. R., Law, K. S., and Thorp, T.: Local Arctic air pollution: A neglected but serious problem, Earth's
548 Future, https://doi.org/10.1029/2018EF000952, 2018.

549 Schmale, J., Zieger, P., and Ekman, A. M. L.: Aerosols in current and future Arctic climate, Nat. Clim. Chang., 11, 95–105,
550 https://doi.org/10.1038/s41558-020-00969-5, 2021.

551 Selimovic, V., Yokelson, R. J., McMeeking, G. R., and Coefield, S.: In situ measurements of trace gases, PM, and aerosol
552 optical properties during the 2017 NW US wildfire smoke event, Atmos. Chem. Phys., 19, 3905–3926,
553 https://doi.org/10.5194/acp-19-3905-2019, 2019.

554 Sierra-Hernández, M. R., Beaudon, E., Porter, S. E., Mosley-Thompson, E., and Thompson, L. G.: Increased fire activity in
555 Alaska since the 1980s: Evidence from an ice core-derived black carbon record, J. Geophys. Res., 127,
556 https://doi.org/10.1029/2021jd035668, 2022.

557 Sinha, P. R., Kondo, Y., Koike, M., Ogren, J. A., Jefferson, A., Barrett, T. E., Sheesley, R. J., Ohata, S., Moteki, N., Coe, H.,
558 Liu, D., Irwin, M., Tunved, P., Quinn, P. K., and Zhao, Y.: Evaluation of ground-based black carbon measurements by filter-
559 based photometers at two Arctic sites, J. Geophys. Res., 122, 3544–3572, https://doi.org/10.1002/2016jd025843, 2017.

560 Skamarock, W. C., Klemp, J. B., Dudhia, J., Gill, D. O., Liu, Z., Berner, J., Wang, W., Powers, J. G., Duda, M. G., Barker, D.
561 M., and Others: A description of the advanced research WRF model version 4, National Center for Atmospheric Research:
562 Boulder, CO, USA, 145, 2019.

563 Stein, A. F., Draxler, R. R., Rolph, G. D., Stunder, B. J. B., Cohen, M. D., and Ngan, F.: NOAA's HYSPLIT Atmospheric
564 Transport and Dispersion Modeling System, Bull. Am. Meteorol. Soc., 96, 2059–2077, https://doi.org/10.1175/BAMS-D-14-
565 00110.1, 2015.

566 Stohl, A., Andrews, E., Burkhart, J. F., Forster, C., Herber, A., Hoch, S. W., Kowal, D., Lunder, C., Mefford, T., Ogren, J. A.,
567 Sharma, S., Spichtinger, N., Stebel, K., Stone, R., Ström, J., Tørseth, K., Wehrli, C., and Yttri, K. E.: Pan-Arctic enhancements

568 of light absorbing aerosol concentrations due to North American boreal forest fires during summer 2004, J. Geophys. Res.,
569 111, https://doi.org/10.1029/2006jd007216, 2006.

570 Taketani, F., Miyakawa, T., Takashima, H., Komazaki, Y., Pan, X., Kanaya, Y., and Inoue, J.: Shipborne observations of
571 atmospheric black carbon aerosol particles over the Arctic Ocean, Bering Sea, and North Pacific Ocean during September
572 2014, J. Geophys. Res., 121, 1914–1921, https://doi.org/10.1002/2015jd023648, 2016.

573 Taketani, F., Miyakawa, T., Takigawa, M., Yamaguchi, M., Komazaki, Y., Mordovskoi, P., Takashima, H., Zhu, C., Nishino,
574 S., Tohjima, Y., and Others: Characteristics of atmospheric black carbon and other aerosol particles over the Arctic Ocean in
575 early autumn 2016: Influence from biomass burning as assessed with observed microphysical properties and model simulations,
576 Sci. Total Environ., 848, 157671, 2022.

577 Thackeray, C. W. and Hall, A.: An emergent constraint on future Arctic sea-ice albedo feedback, Nat. Clim. Chang., 9, 972–
578 978, https://doi.org/10.1038/s41558-019-0619-1, 2019.

579 Vasileva, Moiseenko, and Skorokhod: Emission ratios of trace gases and particles for Siberian forest fires on the basis of
580 mobile ground observations, Atmos. Clim. Sci., 2017.

581 Wang, H., Rasch, P. J., Easter, R. C., Singh, B., Zhang, R., Ma, P.-L., Qian, Y., Ghan, S. J., and Beagley, N.: Using an explicit
582 emission tagging method in global modeling of source-receptor relationships for black carbon in the Arctic: Variations, sources,
583 and transport pathways, J. Geophys. Res., 119, 12,888-12,909, https://doi.org/10.1002/2014jd022297, 2014.

584 Wang, Q., Jacob, D. J., Fisher, J. A., Mao, J., Leibensperger, E. M., Carouge, C. C., Le Sager, P., Kondo, Y., Jimenez, J. L.,
585 Cubison, M. J., and Doherty, S. J.: Sources of carbonaceous aerosols and deposited black carbon in the Arctic in winter-spring:
586 implications for radiative forcing, Atmos. Chem. Phys., 11, 12453–12473, https://doi.org/10.5194/acp-11-12453-2011, 2011.

587 van der Werf, G. R., Randerson, J. T., Giglio, L., van Leeuwen, T. T., Chen, Y., Rogers, B. M., Mu, M., van Marle, M. J. E.,
588 Morton, D. C., Collatz, G. J., Yokelson, R. J., and Kasibhatla, P. S.: Global fire emissions estimates during 1997–2016, Earth
589 Syst. Sci. Data, 9, 697–720, https://doi.org/10.5194/essd-9-697-2017, 2017.

590 van der Werf, G., Randerson, J. T., Giglio, L., Chen, Y., Rogers, B. M., and Van Leeuwen, T. T.: Global Fire Emissions
591 Database version 4 (GFED4), GC33D-0545, 2014.

592 Whaley, C. H., Mahmood, R., von Salzen, K., Winter, B., Eckhardt, S., Arnold, S., Beagley, S., Becagli, S., Chien, R.-Y.,
593 Christensen, J., and Others: Model evaluation of short-lived climate forcers for the Arctic Monitoring and Assessment
594 Programme: a multi-species, multi-model study, Atmos. Chem. Phys., 22, 5775–5828, 2022.

595 Wiggins, E. B., Soja, A. J., Gargulinski, E., Halliday, H. S., Pierce, R. B., Schmidt, C. C., Nowak, J. B., DiGangi, J. P., Diskin,
596 G. S., Katich, J. M., Perring, A. E., Schwarz, J. P., Anderson, B. E., Chen, G., Crosbie, E. C., Jordan, C., Robinson, C. E.,
597 Sanchez, K. J., Shingler, T. J., Shook, M., Thornhill, K. L., Winstead, E. L., Ziemba, L. D., and Moore, R. H.: High temporal
598 resolution satellite observations of fire radiative power reveal link between fire behavior and aerosol and gas emissions,
599 Geophys. Res. Lett., 47, https://doi.org/10.1029/2020gl090707, 2020.

600 Xie, A., Zhu, J., Kang, S., Qin, X., Xu, B., and Wang, Y.: Polar amplification comparison among Earth's three poles under
601 different socioeconomic scenarios from CMIP6 surface air temperature, Sci. Rep., 12, 16548, https://doi.org/10.1038/s41598-
602 022-21060-3, 2022.

603 Xu, J.-W., Martin, R. V., Morrow, A., Sharma, S., Huang, L., Leaitch, W. R., Burkart, J., Schulz, H., Zanatta, M., Willis, M.
604 D., Henze, D. K., Lee, C. J., Herber, A. B., and Abbatt, J. P. D.: Source attribution of Arctic black carbon constrained by
605 aircraft and surface measurements, Atmos. Chem. Phys., 17, 11971–11989, https://doi.org/10.5194/acp-17-11971-2017, 2017.

606   Yurganov, L. N., Jaffe, D. A., Pullman, E., and Novelli, P. C.: Total column and surface densities of atmospheric carbon
607   monoxide in Alaska, 1995, J. Geophys. Res., 103, 19337–19345, https://doi.org/10.1029/97jd02299, 1998.

608   Zhu, C., Kanaya, Y., Takigawa, M., Ikeda, K., Tanimoto, H., Taketani, F., Miyakawa, T., Kobayashi, H., and Pisso, I.:
609   FLEXPART v10.1 simulation of source contributions to Arctic black carbon, Atmos. Chem. Phys., 20, 1641–1656,
610   https://doi.org/10.5194/acp-20-1641-2020, 2020.

611